



Published in final edited form as:

Nat Genet. 2012 October ; 44(10): 1161–1165. doi:10.1038/ng.2398.

A direct characterization of human mutation based on microsatellites

James X. Sun^{1,2}, Agnar Helgason^{3,4}, Gisli Masson³, Sigrí ur Sunna Ebenesersdóttir³, Heng Li^{2,5}, Swapan Mallick², Sante Gnerre⁵, Nick Patterson⁵, Augustine Kong³, David Reich^{2,5}, and Kari Stefansson^{3,6}

¹Division of Health Sciences and Technology, Massachusetts Institute of Technology, Cambridge, MA, USA ²Department of Genetics, Harvard Medical School, Boston, MA, USA ³deCODE Genetics, 101 Reykjavik, Iceland ⁴Department of Anthropology, University of Iceland, Reykjavik, Iceland ⁵Broad Institute, Cambridge, MA, USA ⁶Faculty of Medicine, University of Iceland, Reykjavik, Iceland

Abstract

Mutations are the raw material of evolution, but have been difficult to study directly. We report the largest study of new mutations to date: 2,058 germline changes discovered by analyzing 85,289 Icelanders at 2,477 microsatellites. The paternal-to-maternal mutation rate ratio is 3.3, and the rate in fathers doubles from age 20 to 58 whereas there is no association with age in mothers. Longer microsatellite alleles are more mutagenic and tend to decrease in length, whereas the opposite is seen for shorter alleles. We use these empirical observations to build a model that we apply to individuals for whom we have both genome sequence and microsatellite data, allowing us to estimate key parameters of evolution without calibration to the fossil record. We infer that the sequence mutation rate is $1.4\text{--}2.3 \times 10^{-8}$ per base pair per generation (90% credible interval), and that human-chimpanzee speciation occurred 3.7–6.6 million years ago.

The largest studies of human germline mutation to date have focused on whole-genome sequencing of nuclear families^{1–3} and identified more than a hundred new mutations. However, too few mutations were detected and too few families studied to provide a detailed

Users may view, print, copy, download and text and data- mine the content in such documents, for the purposes of academic research, subject always to the full Conditions of use: http://www.nature.com/authors/editorial_policies/license.html#terms

Correspondence should be addressed to J.X.S. (xinsun@mit.edu), D.R. (reich@genetics.med.harvard.edu), or K.S. (kari.stefansson@decode.is).

Author Contributions

JXS, AH, GM, and DR conceived and performed the research. AH, GM, AK, DR, and KS jointly supervised the study, with AH being the coordinator at deCODE Genetics and DR at Harvard Medical School. AH and GM prepared the raw microsatellite data. JXS, AH, and SSE designed and analyzed the re-genotyping, re-sequencing, and electropherogram re-checking experiments; AH analyzed next generation sequencing data to independently validate mutations. JXS, AH, NP, AK, and DR designed and analyzed the microsatellite modeling and the statistics. SM, HL, and JXS processed and extracted sequence data for the 23 HapMap individuals. SM, SG, and DR performed the analyses of human-chimpanzee genetic divergence and developed the prior distributions relevant to human-chimpanzee speciation. The paper was written primarily by JXS, AH, and DR. The supplementary information was written by JXS and DR.

Data Access

The informed consents associated with the samples at deCODE Genetics specify that genotypes cannot be shared outside of Iceland. However, researchers who wish to re-analyze the data can visit deCODE Genetics to perform these analyses by arrangement with K. Stefansson.

characterization of the mutation process⁴⁻⁷. One outcome of understanding the mutation process would be a direct estimate of the rate of ticking of the molecular clock, which would make it possible to estimate dates from genetic data without relying on the fossil record for calibration.

Here we focus on microsatellites: 1–6 base pair motifs that vary in the number of times they repeat. Due to DNA polymerase slippage during replication, the mutation rate of microsatellites is around 10^{-4} to 10^{-3} per locus per generation⁸⁻¹², far higher than the nucleotide substitution rate of 10^{-8} . We analyzed 2,477 autosomal microsatellites that had been genotyped as part of linkage-based disease gene mapping studies and h were ascertained to be highly polymorphic¹³. The data set included 85,289 Icelanders from 24,832 father-mother-child trios, after restricting to individuals genotyped for at least half of these loci and without evidence of inaccurate parental assignment (Online Methods, Supplementary Figure 1). The median genotype error rate was 1.8×10^{-3} per allele (Supplementary Figure 2, Supplementary Note), high compared to the mutation rate, and thus we took additional steps to reduce the error.

To distinguish genuine mutations from genotype errors, we used two approaches (Online Methods, Supplementary Note). In the ‘trio’ approach (Figure 1A), we identified 1,695 mutations in 5,085,672 transmissions by restricting to instances in which each member of the trio was genotyped more than once. In the ‘family’ approach (Figure 1B), we identified 363 mutations in 952,632 transmissions, validating new mutations by requiring them to be seen in at least one of the proband’s children, and validating ancestral alleles by requiring them to be seen in all of the proband’s siblings (in the family approach, we also used haplotypes of nearby microsatellites to determine the parental origin of mutations; Online Methods, Supplementary Note). The trio and family approaches produced indistinguishable inferences about the mutation process (Table 1, Supplementary Figure 3, Supplementary Figure 4), and hence we combined the data for subsequent analysis (62 mutations were counted twice due to overlap).

To estimate the proportion of candidate mutations that are real, we re-genotyped samples of 103 trio mutations and 99 family mutations leading to false-positive rate estimates of 2.9% and 2.6% respectively (Supplementary Table 1, Supplementary Figure 5). We also estimated the false-positive rate due to errors in the allele-calling algorithm to be 4.3% by manually re-scoring the electropherograms of 316 individuals from the family dataset, and declaring a false-positive if there was disagreement. Combining the two modes, we estimate a 7.2% false-positive rate (Supplementary Table 1). We also obtained an entirely independent estimate by analyzing next-generation sequencing data from the proband and the transmitting parent for 14 candidate mutations for which we had such data, allowing us to validate all but one leading to an estimated false positive rate of 7.1% (Supplementary Table 2). The false-negative rate (probability of an undetected real mutation) was estimated to be 9.0% by simulating mutations and recording the fraction that we failed to detect (Online Methods).

The estimated mutation rate of tetra-nucleotides is 10.01×10^{-4} per locus per generation, 3.7 times higher than the di-nucleotide rate of 2.73×10^{-4} (Table 1). Estimates are nearly

unchanged after correcting for false-positives and false-negatives by $(1-0.072)/(1-0.090)$, and thus we quote unadjusted rates in what follows. Our estimate of the male-to-female mutation rate ratio is $\alpha=3.3$ (95% CI 2.9–3.7) (Supplementary Table 3), within the range of 2–7 previously inferred for sequence substitutions^{4,14,3,15}. Paternal age is correlated with mutation rate ($P=9.3\times 10^{-5}$), whereas maternal age is not ($P=0.47$; Figure 2A, Supplementary Figure 6), consistent with observations based on disease-causing mutations, and the fact that male germ cells undergo numerous mitoses as a man ages, whereas female oocytes do not undergo postnatal cell division⁴.

These data allow the first high resolution direct characterization of the mutation process for the highly polymorphic di- and tetra-nucleotide microsatellites that are typically genotyped⁸. First, 32% of mutations at di-nucleotide microsatellites are multi-step, compared to 1% in tetra-nucleotides (Figure 2B, Supplementary Figure 3) (this explains why the variance of allele length distribution at the tetra-nucleotides is similar to that of di-nucleotides despite their 3.7-fold higher mutation rate^{16,17}). Second, mutation rate increases with allele length^{18,19}, quadrupling between 30–70 bp for di-nucleotides and 40–120 bp for tetra-nucleotides (both tests significant at $P<0.002$) (Figure 2C). Third, loci with uniform repeat structures (e.g. CACACACA) have a 40% higher rate ($P=3\times 10^{-7}$) than compound repeat structures (e.g. CACATCACA), consistent with less DNA polymerase slippage for interrupted tandem repeats^{8,20} (Supplementary Figure 7). Fourth, we detect length constraints^{21,22}, with shorter alleles tending to mutate to become longer and vice versa ($P=2\times 10^{-15}$) (Figure 2D, Supplementary Figure 8, Supplementary Figure 9^{20,23,24}). This pattern contrasts with tri-nucleotide repeat disorders, where long alleles tend to get even longer¹⁹. Fifth, mutation rate correlates ($P<10^{-4}$) with motif length, repeat number, allele-size, distance from exons, gender, and age, but not with recombination rate, distance from telomeres, human-chimpanzee divergence, or parental heterozygosity (Supplementary Table 4; Supplementary Table 5; Supplementary Note).

Microsatellites have been widely used for making inferences about evolutionary history. However, the accuracy of these inferences has been limited by a poor understanding of the mutation process. We developed a new model of microsatellite evolution (Supplementary Note). This model can estimate the time to the most recent common ancestor (TMRCA) between two samples at a microsatellite by taking into account: (1) the dependence of mutation rate on allele length and parental age (Figure 2A,C); (2) the step-size of mutations (Figure 2B); (3) the size constraints on allele length (Figure 2D, Supplementary Figure 8, Supplementary Figure 9); and (4) the variation in generation interval over history. In contrast to the Generalized Stepwise Mutation Model (GSMM), which predicts a linear increase of average squared distance (ASD) between microsatellite alleles over time, the new model predicts a sub-linear increase (Figure 3) and saturation of the molecular clock, due to the constraints on allele lengths. We also extended the model to estimate the sequence mutation rate, using the per-nucleotide diversity flanking each microsatellite as an additional datum. To implement the model, we used a Bayesian hierarchical approach, first generating global parameters common to all loci, followed by locus-specific parameters, and finally the microsatellite alleles at each locus (Online Methods). We used Markov Chain Monte Carlo to infer TMRCA and sequence mutation rate.

We validated the model in three ways (Online Methods). First, we simulated datasets in which we know the true sequence mutation rate and TMRCA, and found that our model is unbiased in estimating sequence mutation rate while producing accurate estimates of the standard error (Supplementary Note). Second, we carried out sensitivity analyses by perturbing model parameters and found that our key inferences are robust (Supplementary Note, Supplementary Figure 10). Third, we empirically validated the model by analyzing 23 individuals for whom we had both microsatellite genotypes and whole genome sequence (WGS) data², and comparing the ASD to the surrounding sequence heterozygosity as a surrogate for TMRCA. The ASD predicted by our model is similar to the empirical curve (Figure 3, Supplementary Figure 11)

Our approach allows inference of evolutionary parameters without calibration to the fossil record. Using the empirical ASD at the di-nucleotide microsatellites in each of the 23 individuals of European, East Asian and sub-Saharan African ancestry for whom we had WGS sequence data (Online Methods), and comparing the ASD to local heterozygosity and human-macaque divergence (as a surrogate for the local mutation rate; Online Methods), we inferred a sequence mutation rate and the TMRCA averaged across the genome (Table 2). We also inferred a 90% credible interval (CI) based on a Bayesian approach integrating over uncertainty in the model parameters (Online Methods; Supplementary Note, Supplementary Table 6). Empirically, mutation rates tend to be more similar within than between populations (Supplementary Table 7; Supplementary Figure 12). The differences across populations are not likely to be due to poor modeling of demographic history, as when we model more realistic histories involving two bottlenecks in non-Africans we obtain the same results (Supplementary Figure 13). The mutation rate differences between populations may be due to shared history, but they are not significant, so we pooled our data across the 23 individuals to produce a sequence mutation rate estimate of 1.82×10^{-8} per bp per generation (90% CI $1.40\text{--}2.28 \times 10^{-8}$ /bp/generation, Table 2) (the confidence interval takes into account correlations in the 23 peoples' histories through a jackknife) (Online Methods).

Our inference of the sequence mutation rate is consistent with Nachman and Crowell's estimate of $\mu_{seq} = 1.3\text{--}2.7 \times 10^{-8}$ /bp/generation based on calibration to the fossil record⁶. It is also consistent with Kondrashov's direct estimate of $\mu_{seq} = 1.8 \times 10^{-8}$ /bp/generation²⁵ from studies of disease causing genes. However, the lower bound of our 90% CI is higher than two recent studies based on whole-genome sequencing (WGS): $\mu_{seq} = 1.1 \times 10^{-8}$ /bp/generation based on 28 sequence mutations detected in a four member family¹, and $\mu_{seq} = 1.0 \times 10^{-8}$ and 1.2×10^{-8} /bp/generation based on 84 sequence mutations detected in two trios^{2,3}. We considered the possibility that this discrepancy might be due to ascertainment bias, because the microsatellites we analyzed were selected to be highly polymorphic (for disease gene mapping) which could cause a too-high ASD. However, this would overestimate TMRCA at the loci we analyzed and thus underestimate the mutation rate, opposite to what would be necessary to explain the discrepancy (Supplementary Figure 12 and Supplementary Note). We hypothesize that the lower mutation rate estimates from the WGS studies might be due to: (i) the limited number of mutations detected in the WGS studies which explains why their confidence intervals overlap ours, (ii) possible underestimation of the false-negative rate in the WGS studies, or (iii) variability in the

mutation rate across individuals so that a few families cannot provide a reliable estimate of the population-wide rate. There is already empirical evidence for variability in the mutation process across individuals: in one trio analyzed in the 1000 Genomes Project study⁸, the father transmitted 92% of the mutations, while in the other trio the father transmitted 36%. Studies of sequence substitution in many families are important, as they will make it possible to measure population-wide rates and study features of the sequence substitution process not accessible to microsatellite analysis.

Our direct estimation of the microsatellite mutation rate, combined with comparative genomics data, also allows us to estimate the date of human-chimpanzee speciation τ_{HC} , which we define as the date of last gene flow between human and chimpanzee ancestors^{26,27}. We estimate a genome-wide average human-chimpanzee genetic divergence time $t_{HC} = 5.80\text{--}9.77$ Mya²⁸ (Online Methods; Table 2). By definition, this must be older than the speciation date τ_{HC} . We then inferred the human-chimpanzee speciation to be $\tau_{HC} = 3.75\text{--}6.57$ Mya by integrating our posterior distribution on t_{HC} with a prior distribution on τ_{HC}/t_{HC} of 0.663 ± 0.041 whose mean we obtained by modeling-based estimates of $\tau_{HC}/t_{HC} = 0.61\text{--}0.68$ ^{29,30}, and whose 95th percentile upper bound of <0.73 we obtained by analyzing human-chimpanzee sequence data in regions with a reduced divergence compared to the autosomal average due to being (1) on chromosome X, (2) in proximity to genes, and (3) near divergent sites that cluster humans and chimpanzees to the exclusion of gorilla (Supplementary Note). Our upper bound of $\tau_{HC} < 6.57$ Mya is lower than the $6.8\text{--}7.2$ Mya³¹ date estimate for *Sahelanthropus tchadensis*, a fossil interpreted as being on the human lineage after the final separation of human and chimpanzee ancestors³² because it shares derived features with other hominins such as bipedal posture, reduced canines and expanded post-canines with thicker enamel³³. In the Supplementary Note, we also obtain an independent upper bound on the human-chimpanzee speciation date of $\tau_{HC} < 6.3$ Mya based on calibration to the fossil record of human-orangutan speciation²⁶. A possible explanation for the discrepancy between the genetic and fossil dates is that *Sahelanthropus* was not a hominin, but instead shared independently-derived similarities (homoplasies)³⁴. Alternatively, populations with hominin traits may have continued to exchange genes with chimpanzee ancestors after *Sahelanthropus*²⁶. Finally, the age of *Sahelanthropus*³¹ may be overestimated.

URL: Complete Genomics data: <http://www.completegenomics.com/>.

Online Methods

Data sets

Microsatellite genotypes were obtained at deCODE Genetics using DNA extracted from blood, and multiplexed capillary gel electrophoresis with automated allele calling¹³. We restricted to 2,477 autosomal loci that were genotyped most heavily (all had a minimum repeat length of 5 units). We analyzed 85,289 individuals genotyped for at least half of these loci, from which we identified 25,067 mother-father-offspring trios using the deCODE Genetics genealogical database (Íslendingabók).

To filter out trios with inaccurate parental assignments, we computed the fraction of loci where both alleles differ between a parent and a child. We empirically set the threshold to filter out almost all known uncle-proband and aunt-proband pairs while retaining almost all known parent-proband pairs (Supplementary Figure 1).

To estimate the per-locus genotyping error rate, we used discordance rates in cases of repeated genotypes (Supplementary Note).

Deep whole genome sequencing data was obtained from two sources. We downloaded 9 sequences generated using Illumina technology, mapping reads using BWA³⁵ and calling SNPs with SAMtools³⁶. We also downloaded 20 Complete Genomics sequences, 6 of which overlap the Illumina sequences (Supplementary Table 7, Supplementary Figure 14). To estimate heterozygosity around each microsatellite, we extracted a window of data centered around it (in most cases, 0.001 centimorgans masking out the central 1kb³⁷; Supplementary Figure 15),

Detecting mutations

For the trio approach, we restricted to transmissions in which all members of the trio were genotyped at least twice and searched for Mendelian inheritance incompatibilities. There were some detected mutations in which the parental origin was ambiguous (Supplementary Note), and we included these for analyses of the mutation rate but not for analyses requiring parental origin (Fig 2B). For mutations with unambiguous parental origin, the ancestral allele was defined as the one that was closer in length to the mutant allele (we randomly chose the ancestral allele if both were equally close). We filtered out 49 loci that harbored many more mutations from homozygous parents to homozygous children than expected based on Hardy-Weinberg equilibrium, a phenomenon that affected the trio, but not the family data. We determined that this is a real error mode due to polymorphisms under the PCR primer sites³⁸⁻⁴⁰ by sequencing primer sites from 15 mutations and identifying 5 with SNPs in the primer region (Supplementary Note).

For the family approach, we restricted to transmissions where genotyping was available not just for a proband's two parents, but also for at least one child and one sibling (Figure 1B). We identified putative mutations by searching for Mendelian incompatibilities between the proband and their parents. We used Allegro 2.0⁴¹ to phase the family masking out the mutant locus, using all available loci from the same chromosome. We then assigned the haplotype carrying the mutation to one of the proband's parents (Supplementary Note). To validate the mutation, we required at least one sibling to carry the haplotype with the ancestral allele, no sibling to carry the mutant, and at least one child to carry the haplotype with the mutant.

The trio and family approaches provide complementary information. A bias that only affects the trio approach is somatic mutations in the lineage of genotyped cells but not germline cells transmitted to offspring (this is minimized since the DNA we analyzed was extracted from blood, but is still a concern). A bias that only affects the family-based approach is that mutations in progenitor germ cells might cause a mutation to be observed simultaneously in the proband and its siblings, causing us to reject a real mutation. The fact that both

approaches produce consistent inferences despite the difference biases increases our confidence in the results.

False-positive and false-negative rates

To estimate the false-positive rate, we re-genotyped candidate mutations. In the trio dataset, we randomly re-genotyped 103 mutations. In the family dataset, we targeted mutations that had a higher *a priori* chance of being in error (Supplementary Table 1). To provide an entirely independent estimate of the false-positive rate, we identified 14 candidate mutations where we had at least 7-fold whole genome sequencing data from the proband as well as (at least) the transmitting parent. We then manually examined the data, failing to validate only 1 of the 14 mutations (Supplementary Table 2).

To estimate the false-negative rate (the proportion of genuine mutations that were missed), we randomly distributed mutations on the genealogy and then tested whether they gave rise to detectable inheritance errors. As an example, suppose that the father-mother-proband trio has genotypes of allele-lengths (6 10), (8 10), (8 10), respectively. If the mother passed allele 10 to the proband, and the father passed a 6 → 8 mutation, then this mutation would not be detected.

Statistical characterization of the microsatellite mutation process

To infer the standard error of the mutation rate, taking into account rate variation across loci, we used a hierarchical Bayesian model (Supplementary Note). To infer the number of microsatellite repeats, we started with the amplicon size, which includes not just the repeats but all the sequence between the PCR primers. We then subtracted the span of the flanking sequence inferred from the human genome reference (Supplementary Figure 16). To compute the relative length of an allele, we measured the mean and standard deviation over all individuals at that locus, and report the standard deviations from the mean (Z-score). To estimate motif impurity (Supplementary Figure 7), we applied the Tandem Repeat Finder software to the human genome reference (Supplementary Figure 16). To test for association between the microsatellite mutation process and genomic features (Supplementary Table 4), we performed a logistic regression to mutation rate and directionality, and a Poisson regression to step size. To test for interaction, we performed multivariate logistic regression (Supplementary Table 5).

Prior distributions on evolutionary parameters

For our Bayesian modeling of sequence mutation rate and genetic divergence times, we required prior distributions on evolutionary parameters (Supplementary Table 6):

- *Generation interval*: Based on interviews with experts on chimpanzee and gorilla demographic structure (L Vigilant and K Langergraber), we assume that the ancestral generation time was 22.5 ± 4.2 (mean \pm SD) years. Based on the literature^{42,43} (Supplementary Figure 17), we assume that present-day generation time is 29 ± 2 years. We also assume that the difference between the male and female generation time was 0.5 ± 3.3 years in the ancestral population and 6.0 ± 2.0 today (Supplementary Note). We sample the transition between ancestral to

present-day generation time to be a mixture of 3 equally weighted exponential distributions, with means of 50Kya, 200Kya, and 2Mya, corresponding to hypothetical changes around the Upper Paleolithic revolution, evolution of modern humans, and evolution of *Homo erectus*.

- *Human-ape relative genetic divergences*: From the literature, we assume that the ratio of human-chimpanzee to European-European genetic divergence per base pair is²⁸ 15.400 ± 0.356 , and that the ratio of human-orangutan to human-chimpanzee genetic divergence of 2.650 ± 0.075 .^{26,29} We assume that the molecular process of mutation has been constant over great ape history.
- *Human-chimpanzee speciation time* (τ_{HC}): Human-chimpanzee speciation time is by definition less than human-chimpanzee genetic divergence time. Our prior on τ_{HC}/t_{HC} has a normal distribution with mean 0.663, within the range of 0.61–0.68 from model-based analyses^{29,30}. We use a standard deviation of 0.041 based on an analysis in the Supplementary Note suggesting showing that an upper bound on the ratio of human-chimpanzee speciation to genetic divergence is 0.73 (our prior distribution is set that 95% of its density is below this).

A model of microsatellite evolution assisted by flanking sequence heterozygosity

As a metric of microsatellite allelic divergence between two samples, we use the Average

Squared Distance (ASD). Given allele lengths x_1, x_2, \dots, x_n ,
$$ASD = \frac{1}{n(n-1)} \cdot \sum_{i,j} (x_i - x_j)^2.$$

To model ASD along with flanking sequence heterozygosity, we simulate the evolution of a pair of chromosomes from a common ancestor, over multiple loci and individuals. The model is hierarchical: At the top level, global parameters (Supplementary Table 6) common to all loci are simulated, such as the genome-wide present-day sequence and microsatellite mutation rates, and generation-time effects. One level down, locus-specific mutation rates are computed based on global parameters and locus-specific information. At the third level, for each individual, a two-sample coalescent tree is generated (Supplementary Note).

A potential pitfall in inferring TMRCA with our data is that the microsatellites we analyzed were ascertained to be highly polymorphic in Europeans. This raises two complications. First, the sequence flanking the microsatellites may have a different mutation rate than the genome average, and to correct for this, we compared ASD to the ratio of sequence heterozygosity and human-macaque divergence at each locus (as a surrogate for local mutation rate). Second, ascertainment of highly polymorphic microsatellites can bias toward deeper genealogies than the genome average which in turn can bias average TMRCA to be too high. By studying the sequence flanking the microsatellites, we determined that the trees were on average 1.04 times deeper than the genome average, and we corrected Table 2's estimate of genome-wide average TMRCA by this factor (Supplementary Note, Supplementary Table 8).

To infer sequence mutation rate and TMRCA using the microsatellite evolution model, we use a Markov Chain Monte Carlo (MCMC) following the method of ref. 44 (Supplementary Note). Combining data across individuals is not trivial because of shared history across

individuals. To obtain proper standard errors for the combined mutation rate, we performed a jackknife⁴⁵, where each locus is removed at a time. This gives the final set of standard errors.

Editorial Summary (AOP and Month, same)

David Reich and colleagues report a direct characterization of the human mutation rate based on analysis of 85,289 Icelandic individuals genotyped at 2,477 autosomal microsatellite loci. They use this to build a model of microsatellite evolution and estimate key evolutionary parameters.

Supplementary Material

Refer to Web version on PubMed Central for supplementary material.

Acknowledgments

We thank DF Gudbjartsson for advice on running Allegro 2.0; J Fenner, J Hawks, K Langergraber, D Pilbeam and L Vigilant for discussions that informed the prior distributions on evolutionary parameters; and Y Erlich, M Gymrek, D Lieberman, B Payseur, D Pilbeam, A Siepel, S Sunyaev, and anonymous reviewers for critiques. This work was supported by a Bioinformatics and Integrative Genomics PhD training grant (JXS), a Burroughs Wellcome Travel Grant (JXS), a Burroughs Wellcome Career Development Award in the Biomedical Sciences (DR), a HUSEC seed grant from Harvard University (DR), a SPARC award from the Broad Institute of Harvard and MIT (DR), a National Science Foundation HOMINID grant 1032255 (DR), and a National Institute of Health grant R01HG006399 (DR).

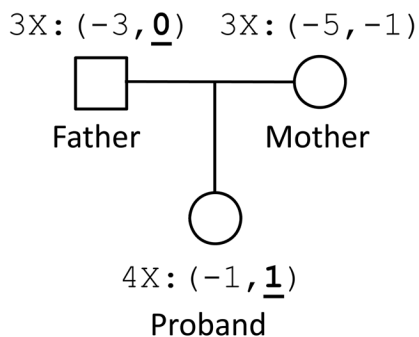
References

1. Roach JC, et al. Analysis of genetic inheritance in a family quartet by whole-genome sequencing. *Science*. 2010; 328:636–9. [PubMed: 20220176]
2. Durbin RM, et al. A map of human genome variation from population-scale sequencing. *Nature*. 2010; 467:1061–73. [PubMed: 20981092]
3. Conrad DF, et al. Variation in genome-wide mutation rates within and between human families. *Nature genetics*. 2011; 43:712–714. [PubMed: 21666693]
4. Crow JF. The origins, patterns and implications of human spontaneous mutation. *Nat Rev Genet*. 2000; 1:40–7. [PubMed: 11262873]
5. Crow JF. Age and sex effects on human mutation rates: an old problem with new complexities. *J Radiat Res (Tokyo)*. 2006; 47 (Suppl B):B75–82. [PubMed: 17019055]
6. Nachman MW, Crowell SL. Estimate of the mutation rate per nucleotide in humans. *Genetics*. 2000; 156:297–304. [PubMed: 10978293]
7. Arnheim N, Calabrese P. Understanding what determines the frequency and pattern of human germline mutations. *Nat Rev Genet*. 2009; 10:478–88. [PubMed: 19488047]
8. Ellegren H. Microsatellites: simple sequences with complex evolution. *Nat Rev Genet*. 2004; 5:435–45. [PubMed: 15153996]
9. Weber JL, Wong C. Mutation of human short tandem repeats. *Hum Mol Genet*. 1993; 2:1123–8. [PubMed: 8401493]
10. Xu X, Peng M, Fang Z. The direction of microsatellite mutations is dependent upon allele length. *Nat Genet*. 2000; 24:396–9. [PubMed: 10742105]
11. Whittaker JC, et al. Likelihood-based estimation of microsatellite mutation rates. *Genetics*. 2003; 164:781–7. [PubMed: 12807796]
12. Huang QY, et al. Mutation patterns at dinucleotide microsatellite loci in humans. *Am J Hum Genet*. 2002; 70:625–34. [PubMed: 11793300]

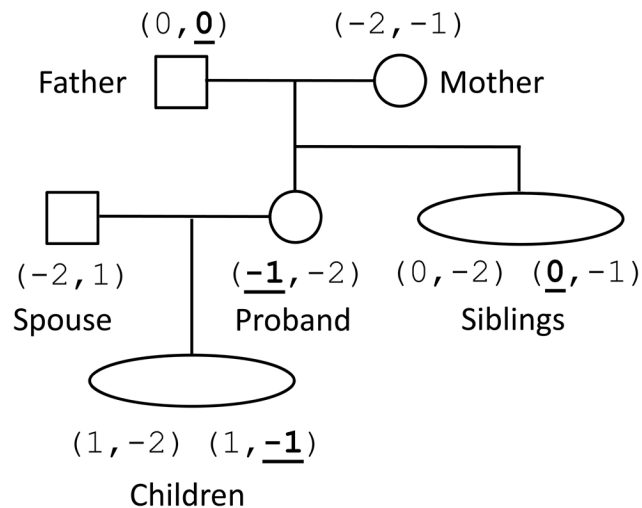
13. Kong A, et al. A high-resolution recombination map of the human genome. *Nat Genet.* 2002; 31:241–7. [PubMed: 12053178]
14. Makova KD, Li WH. Strong male-driven evolution of DNA sequences in humans and apes. *Nature.* 2002; 416:624–6. [PubMed: 11948348]
15. Lynch M. Rate, molecular spectrum, and consequences of human mutation. *Proc Natl Acad Sci U S A.* 2010; 107:961–8. [PubMed: 20080596]
16. Slatkin M. A measure of population subdivision based on microsatellite allele frequencies. *Genetics.* 1995; 139:457–62. [PubMed: 7705646]
17. Goldstein DB, Ruiz Linares A, Cavalli-Sforza LL, Feldman MW. An evaluation of genetic distances for use with microsatellite loci. *Genetics.* 1995; 139:463–71. [PubMed: 7705647]
18. Ballantyne KN, et al. Mutability of Y-chromosomal microsatellites: rates, characteristics, molecular bases, and forensic implications. *Am J Hum Genet.* 2010; 87:341–53. [PubMed: 20817138]
19. Cummings CJ, Zoghbi HY. Fourteen and counting: unraveling trinucleotide repeat diseases. *Hum Mol Genet.* 2000; 9:909–16. [PubMed: 10767314]
20. Kruglyak S, Durrett RT, Schug MD, Aquadro CF. Equilibrium distributions of microsatellite repeat length resulting from a balance between slippage events and point mutations. *Proc Natl Acad Sci U S A.* 1998; 95:10774–8. [PubMed: 9724780]
21. Zhivotovsky LA, Feldman MW, Grishechkin SA. Biased mutations and microsatellite variation. *Mol Biol Evol.* 1997; 14:926–33. [PubMed: 9287425]
22. Feldman MW, Bergman A, Pollock DD, Goldstein DB. Microsatellite genetic distances with range constraints: analytic description and problems of estimation. *Genetics.* 1997; 145:207–16. [PubMed: 9017402]
23. Sainudiin R, Durrett RT, Aquadro CF, Nielsen R. Microsatellite mutation models: insights from a comparison of humans and chimpanzees. *Genetics.* 2004; 168:383–95. [PubMed: 15454551]
24. Garza JC, Slatkin M, Freimer NB. Microsatellite allele frequencies in humans and chimpanzees, with implications for constraints on allele size. *Mol Biol Evol.* 1995; 12:594–603. [PubMed: 7659015]
25. Kondrashov AS. Direct estimates of human per nucleotide mutation rates at 20 loci causing Mendelian diseases. *Hum Mutat.* 2003; 21:12–27. [PubMed: 12497628]
26. Patterson N, Richter DJ, Gnerre S, Lander ES, Reich D. Genetic evidence for complex speciation of humans and chimpanzees. *Nature.* 2006; 441:1103–8. [PubMed: 16710306]
27. Steiper ME, Young NM. Primate molecular divergence dates. *Molecular phylogenetics and evolution.* 2006; 41:384–94. [PubMed: 16815047]
28. Green RE, et al. A draft sequence of the Neandertal genome. *Science.* 2010; 328:710–22. [PubMed: 20448178]
29. Burgess R, Yang Z. Estimation of hominoid ancestral population sizes under bayesian coalescent models incorporating mutation rate variation and sequencing errors. *Mol Biol Evol.* 2008; 25:1979–94. [PubMed: 18603620]
30. McVicker G, Gordon D, Davis C, Green P. Widespread genomic signatures of natural selection in hominid evolution. *PLoS genetics.* 2009; 5:e1000471. [PubMed: 19424416]
31. Lebatard AE, et al. Cosmogenic nuclide dating of Sahelanthropus tchadensis and Australopithecus bahrelghazali: Mio-Pliocene hominids from Chad. *Proceedings of the National Academy of Sciences of the United States of America.* 2008; 105:3226–31. [PubMed: 18305174]
32. Brunet M, et al. A new hominid from the Upper Miocene of Chad, Central Africa. *Nature.* 2002; 418:145–51. [PubMed: 12110880]
33. Lieberman, DE. *The Evolution of the Human Head.* Belknap Press of Harvard University Press; 2011.
34. Wood B, Harrison T. The evolutionary context of the first hominins. *Nature.* 2011; 470:347–52. [PubMed: 21331035]
35. Li H, Durbin R. Fast and accurate short read alignment with Burrows-Wheeler transform. *Bioinformatics.* 2009; 25:1754–60. [PubMed: 19451168]

36. Li H, et al. The Sequence Alignment/Map format and SAMtools. *Bioinformatics*. 2009; 25:2078–9. [PubMed: 19505943]
37. Hinch AG, et al. The landscape of recombination in African Americans. *Nature*. 2011; 476:170–5. [PubMed: 21775986]
38. Weber JL, Broman KW. Genotyping for human whole-genome scans: past, present, and future. *Adv Genet*. 2001; 42:77–96. [PubMed: 11037315]
39. Johansson AM, Sall T. The effect of pedigree structure on detection of deletions and other null alleles. *Eur J Hum Genet*. 2008; 16:1225–34. [PubMed: 18414511]
40. Callen DF, et al. Incidence and origin of “null” alleles in the (AC)_n microsatellite markers. *Am J Hum Genet*. 1993; 52:922–7. [PubMed: 8488841]
41. Gudbjartsson DF, Thorvaldsson T, Kong A, Gunnarsson G, Ingolfsdottir A. Allegro version 2. *Nat Genet*. 2005; 37:1015–6. [PubMed: 16195711]
42. Fenner JN. Cross-cultural estimation of the human generation interval for use in genetics-based population divergence studies. *Am J Phys Anthropol*. 2005; 128:415–23. [PubMed: 15795887]
43. Helgason A, Hrafnkelsson B, Gulcher JR, Ward R, Stefansson K. A populationwide coalescent analysis of Icelandic matrilineal and patrilineal genealogies: evidence for a faster evolutionary rate of mtDNA lineages than Y chromosomes. *Am J Hum Genet*. 2003; 72:1370–88. [PubMed: 12721957]
44. Marjoram P, Molitor J, Plagnol V, Tavaré S. Markov chain Monte Carlo without likelihoods. *Proc Natl Acad Sci U S A*. 2003; 100:15324–8. [PubMed: 14663152]
45. Efron B, Gong G. A leisurely look at the bootstrap, the jackknife, and cross-validation. *The American Statistician*. 1983; 37:36–48.

A. TRIO_00343



B. FAM_10390

**Figure 1. Examples of verified mutations from a trio and a family**

The proband is the individual inheriting a mutation, and all individuals are named relative to the proband. All alleles are given in repeat units and shifted so that the ancestral allele has length 0. The mutating allele is underlined. (A) We show a mutation detected using the trio approach. Confirmation of the mutation is from multiple genotyping of the trio: the father, mother, and proband are genotyped 3 \times , 3 \times , and 4 \times , respectively. (B) We show a mutation detected using the family approach. One sibling verified the ancestral allele, and one child verified the mutant allele. The phasing of alleles from the mutant locus and other loci from the same chromosome shows that the sibling with alleles (0,-2) did not inherit the ancestral '0' but rather the other '0' allele from the father.

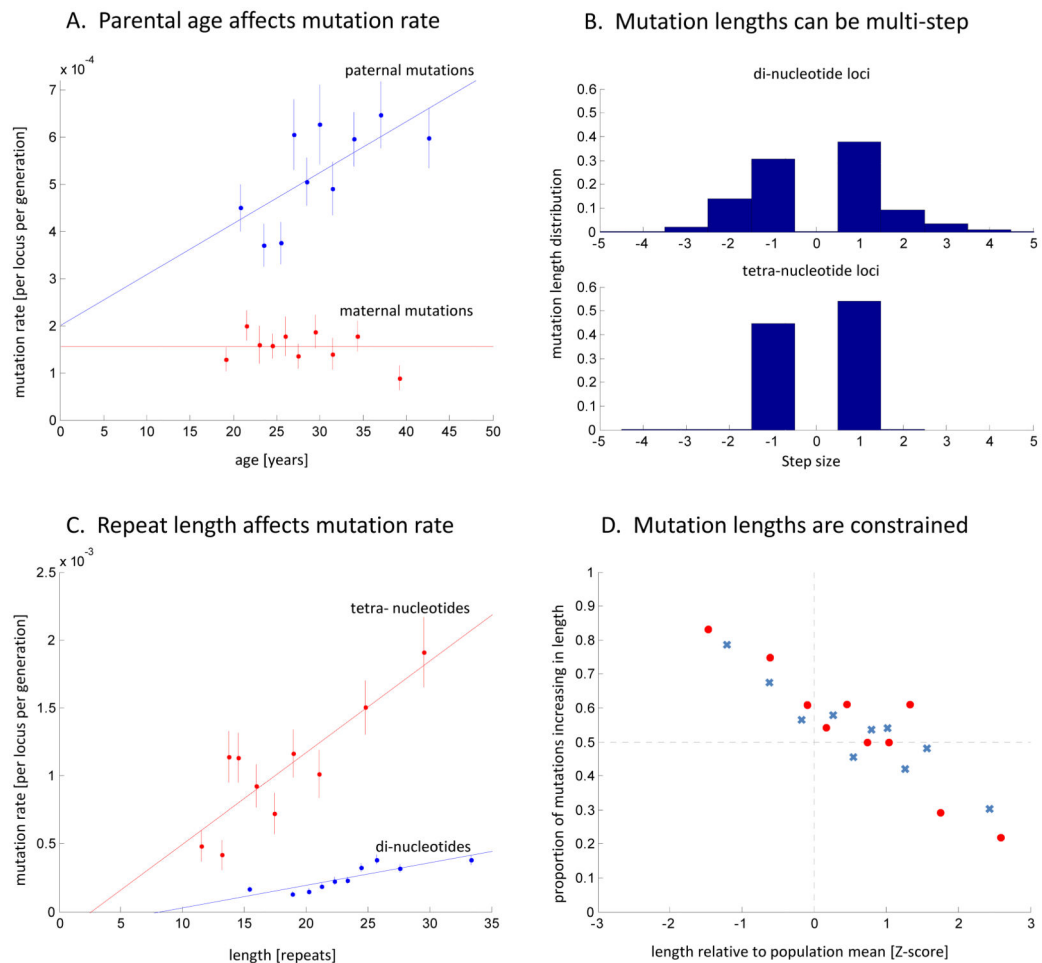


Figure 2. Characteristics of the microsatellite mutation process

(A) Paternal (blue) and maternal (red) mutation rates. The x-axis shows the parental age at child-birth. The data points are grouped into 10 bins (vertical bars show 1 standard error). The paternal rate shows a positive correlation with age (logistic regression of raw data: $P=9.3 \times 10^{-5}$; slope = $1.1 \times 10^{-5}/\text{yr}$), with an estimated doubling of rate from age 20 to 58. The maternal rate shows no evidence of increasing with age ($P=0.47$). (B) Mutation length distributions differ between di- and tetra-nucleotides (upper and lower histograms), with the x-axis in units of step-size. While the di-nucleotide loci experience multi-step mutations in 32% of instances, tetra-nucleotides mutate almost exclusively by a single-step of 4 bases. (C) Mutation rate increases with allele length: di-nucleotides (blue) have a slope of 1.65×10^{-5} per repeat unit ($P=1.3 \times 10^{-3}$) and tetra-nucleotides (red) have a slope of 6.73×10^{-5} per repeat unit ($P=1.8 \times 10^{-3}$). (D) Constraints on allele lengths: When the parental allele is relatively short, mutations tend to increase in length, and when the parental allele is relatively long, mutations tend to decrease in length. Di- and tetra-nucleotides are shown in blue crosses and red circles, respectively. Probit regression of the combined di- and tetra-data shows highly significant evidence of an effect ($P=2.8 \times 10^{-18}$).

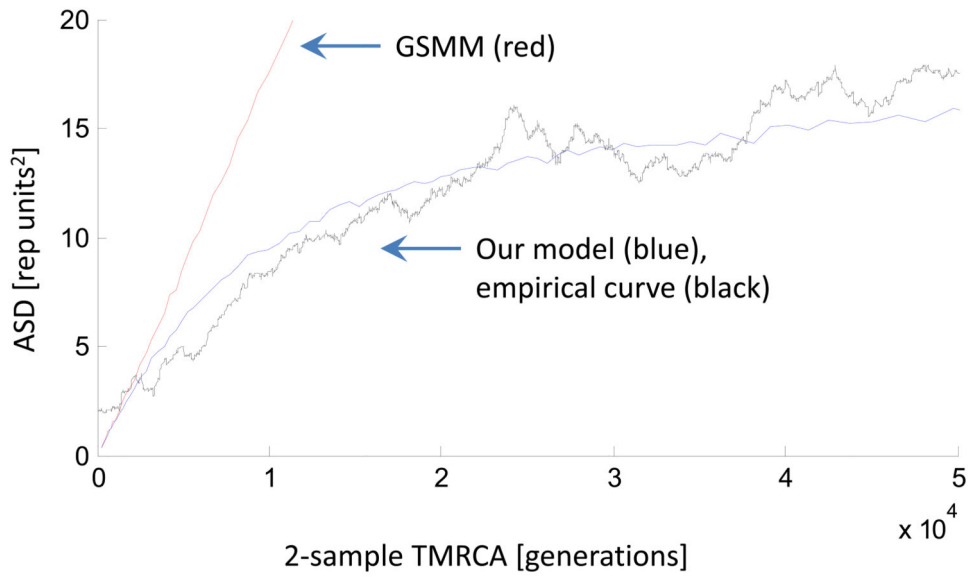


Figure 3. Empirical validation of our model with sequence-based estimates of TMRCA
 In red is the simulation of ASD as a function of TMRCA for the standard random walk (GSMM) model. In blue is the simulation of our model, in which the non-linearity compared to GSMM is primarily due to the length constraint that we empirically observed in microsatellites. In black is the empirically observed ASD at microsatellites in 23 HapMap individuals as a function of sequence-based estimates of TMRCA, which is estimated using $\frac{\theta_{seq}}{2\mu_{seq}}$, where θ_{seq} is the local sequence diversity surrounding each microsatellite locus, and μ_{seq} is 1.82×10^{-8} (obtained from Table 2). The close match of the empirical curve to our model simulations suggests that our model works, and motivates the analysis in which we use the sequence substitution rate in small windows around the microsatellites to make inferences about evolutionary parameters like the sequence mutation rate.

Author Manuscript

Author Manuscript

Author Manuscript

Author Manuscript

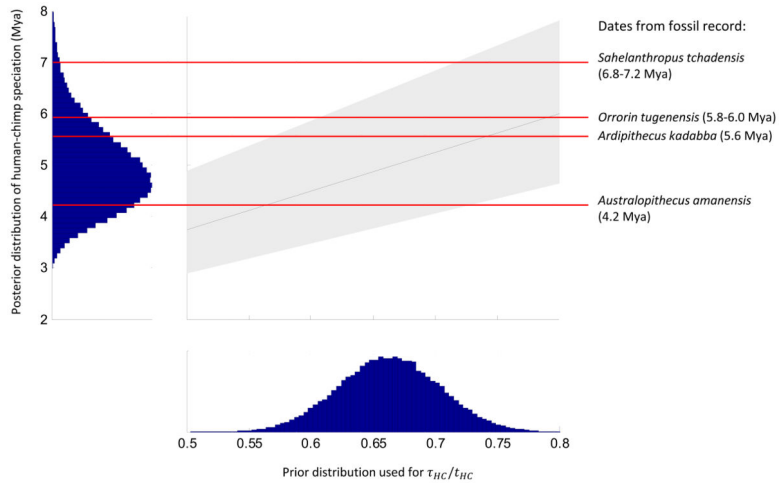


Figure 4. Human-chimpanzee speciation date inferred without a fossil calibration
 In the square panel, we give the 90% Bayesian credible interval for human-chimpanzee speciation time (gray), for a range of values of the ratio of speciation time to divergence time τ_{HC}/t_{HC} . The blue curve shows our prior probability distribution for τ_{HC}/t_{HC} , justified in Supplementary Note. The red horizontal lines are the dates of fossils that are candidates for being on the hominin lineage post-dating the speciation of humans and chimpanzees. *Australopithecus amanensis*, *Orrorin tugenensis* and *Ardipithecus kadabba* are within our plausible speciation times, while *Sahelanthropus tchadensis* pre-dates the inferred speciation time for all plausible values of τ_{HC}/t_{HC} . Our prior distribution for τ_{HC}/t_{HC} is shown in the bottom histogram, and our posterior distribution of human-chimpanzee speciation time is shown in the left histogram.

Author Manuscript

Author Manuscript

Author Manuscript

Author Manuscript

Table 1

Direct estimates of microsatellite mutation rates

	Mutations	Transmissions	Mutation rate ($\times 10^{-4}$) [*]	
			mean	5 th – 95 th percentile
di-nucleotide loci [†]				
Trio-approach	1,218	4,578,348	2.66	2.47 – 2.85
Family-approach	269	861,204	3.12	2.65 – 3.59
Combined	1,487	5,439,552	2.73	2.56 – 2.91
tetra-nucleotide loci				
Trio-approach	380	393,072	9.67	8.44 – 10.89
Family-approach	86	72,516	11.86	8.70 – 15.02
Combined	466	465,588	10.01	8.86 – 11.15

^{*} The 90% credible interval is calculated based on a Bayesian hierarchical beta-binomial model (Supplementary Note), which allows for the mutation rate to vary across loci.

[†] The breakdown of the mutation rate by motif type for di-nucleotides is in Supplementary Table 9.

Table 2

Estimates of mutation rates and human-ape divergence times

	Mean	5 th – 95 th percentile*	mean	5 th – 95 th percentile
Present-day mutation rates	<i>units: per generation per site</i>		<i>units: per year per site</i>	
di-nucleotide microsatellite rate (per locus)	2.73×10^{-4}	$2.56 - 2.91 \times 10^{-4}$	9.47×10^{-6}	$8.29 - 10.82 \times 10^{-6}$
$\hat{\mu}_{seq}$: nucleotide substitution rate (per base)	1.82×10^{-8}	$1.40 - 2.28 \times 10^{-8}$	6.76×10^{-10}	$5.11 - 8.41 \times 10^{-10}$
Genetic divergence times	<i>units: thousand generations ago</i>		<i>units: million years ago</i>	
t_{CEU} : Western Europeans	22.8	17.8 – 29.6	0.546	0.426 – 0.709
t_{YRI} : Yoruba (African)	30.2	23.6 – 39.2	0.720	0.562 – 0.933
t_{HC} : human-chimpanzee	352	272 – 459	7.49	5.80 – 9.77
\bar{t}_{HO} : human-orangutan	932	717 – 1220	19.8	15.2 – 25.9
\bar{t}_{HC} : human-chimpanzee speciation time	233	176 – 309	4.97	3.75 – 6.57

* 90% Bayesian credible interval obtained from the Bayesian posterior distribution.

Author Manuscript

Author Manuscript

Author Manuscript

Author Manuscript